

Laboratory and Commercial Synthesized Zinc Oxide Nanoparticles Adsorption onto Coconut Husk: Characterization, Isotherm, Kinetic, and Thermodynamic Studies

Eric Kwabena Droepenu ^{1,2,*} , Ebenezer Aquisman Asare ^{1,2} , Samuel Boakye Dampare ² , Dennis Kpakpo Adotey ², Alexander Obiri Gyampoh ³, Eugene Kumi-Arhin ⁴

¹ Resource Chemistry Program, Faculty of Resource Science and Technology, Universiti Malaysia Sarawak 94300, Kota Samarahan, Sarawak, Malaysia

² Graduate School of Nuclear and Allied Sciences, University of Ghana, AE1, Kwabenya-Accra, Ghana

³ Departments of Science, Kibi Presbyterian College of Education, Kibi, Eastern Region, Ghana

⁴ Department of Chemistry, School of Physical Science, College of Agriculture and Natural Sciences, University of Cape Coast, Cape Coast, Ghana

* Correspondence: kobladodzie01@yahoo.com;

Scopus Author ID 57216372673

Received: 2.06.2020; Revised: 29.06.2020; Accepted: 30.06.2020; Published: 5.07.2020

Abstract: The accelerating application of zinc oxide nanoparticles (ZnO-NPs) has called for attention to their potential environmental and human health risks. This work aimed to investigate the sorption efficiency of laboratory and commercial synthesized nanocrystalline zinc oxide onto raw coconut husk in a batch adsorption study. Characterization of samples was performed by employing spectroscopies techniques such as X-ray Diffraction Spectroscopy, Field Emission Scanning Electron Microscopy, Transmission Electron Spectroscopy, Fourier transform IR Spectroscopy, and Brunauer–Emmett–Teller. A spherical shaped nanocrystalline ZnO with a mean crystallite and particle size of 14.7 nm and 24 nm by XRD and TEM was synthesized as compared to the commercial ZnO-NPs of size < 50 nm. The maximum percentage removal of 88% (0.13 mg/g) and 90% (0.16 mg/g) for laboratory synthesized and commercial ZnO-NPs respectively was recorded at an optimum contact time of 80 minutes. The data also indicated 2.0 g sorbent mass and pH of 8 as the optimum conditions for maximum percentage removal of these nanoparticles. Both Langmuir and Freundlich models fitted best for laboratory synthesized ZnO-NPs with a maximum capacity of 0.797 mg/g, whereas Langmuir isotherm model alone with a maximum capacity of 0.710 mg/g fitted well for commercial ZnO-NPs. The n-value from the Freundlich model, as well as separation factor (R_L) were greater than unity suggesting a favorable adsorption process. The study obeyed pseudo-second-order, which was exothermic with a high degree of freedom of sorbent-sorbate interaction. The results suggested that coconut husk is potentially scalable for removing ZnO-NPs from wastewater.

Keywords: Zinc oxide nanoparticles; Adsorption studies; Raw coconut husk; Thermodynamic studies; Kinetic studies; Isotherm model.

© 2020 by the authors. This article is an open-access article distributed under the terms and conditions of the Creative Commons Attribution (CC BY) license (<https://creativecommons.org/licenses/by/4.0/>).

1. Introduction

In recent years, nanotechnology has seen significant growth of engineered nanomaterials (ZnO, TiO₂, Ag, CeO₂, SiO₂) in its production [1]. These materials find their application in consumer products, food packaging, and food additives, pharmaceuticals, optical

and electrical devices, photodetectors, photocatalysts, an antifouling pigment in paints, and adsorbents for environmental remediation [2-8]. Through various simulated experiments, it was predicted that the emission concentration of Ti, Ag, and Zn nanoparticles in the environment were in the ranges of 10^{-8} - 10^{-1} , 10^{-8} - 10^{-1} , and 10^{-3} - 10^0 , respectively [9].

Owing to zinc oxide nanoparticles (ZnO-NPs) wide bandgap of 3.37 eV at room temperature and the different morphologies they exhibit, they tend to be used in sunscreens and photocatalysts, due to their excellent absorption of UV radiation [10], antibacterial, anticancer, and antiviral agents due to the different structures they exhibit [11-19]. Despite the importance of these materials in their industrial applications, their potential risk to the environment and public health is another concern when they exceed their threshold concentrations [20-21]. The maximum permissible limit of zinc in drinking water is 2.0 mg/l, as suggested by the Malaysian Environmental Quality Act, 1974.

However, various biological and chemical treatment techniques have been conducted on the removal of these metal ions and nano-sized particles such as chemical precipitation, ion-exchange, reverse osmosis, electroflotation, ultrafiltration, or electrochemical deposition [22-23]. Although these methods contributed tremendously in alleviating these pollutants from water, they are saddled with drawbacks or limitations. Some of these limitations include economic feasibility, less effective treatment of pollutants at lower concentrations, and the creation of a large amount of sludge after the process [24-27]. Meanwhile, adsorption has been universally accepted and demonstrated to be a favorable and feasible alternative for effective pollutant removal from wastewater and water [28]. This is due to its simplicity of design, flexibility in operation, and non-sensitivity to toxic substances due to the nature of the adsorbent used [29]. Industries quest for low-cost operations in water remediation has led to numerous studies to identify low cost and highly efficient sorbents derived from renewable lignocellulose biomass from agricultural by-products such as Pistachio Shell [30], Rubber Seed Shell [31], Moroccan attapulgit [32], Adulsa (*Justicia adhatoda*) Leaves powder [33], willow, paulownia, wheat straw and maize stalks [34], *Canna generalis* [35], coconut shell, *Eucheuma spinosum*, and walnut shell [36-38]. Lignocellulose biomass is known for its economic and environmentally friendly nature, its availability, renewability, and cost-effectiveness [39], which can be used in the raw state, carbonized, or chemically treated state [40-42] to enhance their removal efficiency towards pollutants as indicated by [40]. The high content of cellulose, lignin, and other polar functional groups of lignin such as alcohols, aldehydes, ketones, carboxylic, phenolic, and ether groups in lignocellulose biomass enhance the adsorbent binding ability of pollutants through different binding systems [43].

It is against this backdrop that dry raw coconut husk (RCH) as sorbent material was used in a batch adsorption studies to determine the removal efficiency of two ZnO-NPs. One of the ZnO-NPs was synthesized through a solvothermal technique and characterized (L-ZnO-NPs), whereas the other is a commercial ZnO-NPs purchased from suppliers (C-ZnO-NPs). Characterization of sorbents and sorbate, adsorption kinetics using pseudo-first, pseudo-second and intra-particle diffusion models, adsorption isotherm using Langmuir, Freundlich, and Temkin models as well as thermodynamics parameters were examined to identify the sorption mechanism of the two nanoparticles onto the sorbents. This study was carried out in Kota Samarahan in the Sarawak state of Malaysia from August 2019 to January 2020.

2. Materials and Methods

2.1. Materials.

Chemicals employed in this work are of analytical reagent grade supplied by Sigma Aldrich, India, and VWR Amresco, US. The chemicals include Zinc chloride (ZnCl_2), Nitric acid (HNO_3), absolute ethanol, and sodium hydroxide (NaOH). All solutions used throughout the study were prepared using deionized water (DW).

2.2. Sorbent collection and preparation.

The coconut fruits (Fig. 1) were purchased from the Bandariyyah market, Kota Samarahan, in the Sarawak state of Malaysia. The dry husks obtained from dehusking the fruit were cleaned with tap water followed by air-dried for one week, and then oven-dried at a temperature of 80°C for 6 hours to obtain dry biomass. The dry biomass was ground to a fine powder using a blender (FGR-350) and screened through Retsch Analysensieb sieve mesh of size $210\ \mu\text{m}$ (DIN-ISO 3310/1) on a mechanical shaker (Endecotts EFL 2 mk3 Test Sieve Shaker). The sieved sample (RCH) was stored in zip-lock plastic bags to avoid moisture and fungal infection. Some physicochemical determinations were carried out on RCH sample, which is illustrated in Table 1.

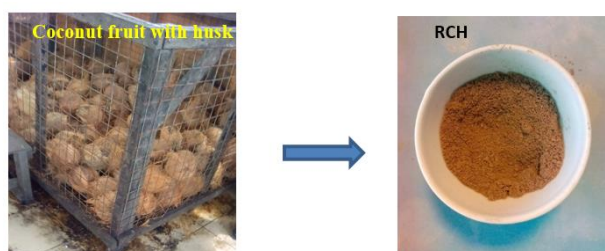


Figure 1. Coconut fruit dehusked and processed into powdered raw coconut husk sorbent (RCH).

2.3. Laboratory synthesis of ZnO-NPs.

The laboratory synthesis of L-ZnO-NPs sample was based on the solvothermal method reported by [44] with slight changes. An amount of $4.08 \pm 0.1\ \text{g}$ ($0.01\ \text{mol}$) of ZnCl_2 was dissolved in 50 mL of absolute ethanol in a 250 mL Schott bottle and heated to a temperature of 60°C with constant stirring using electrical stirring hotplate (Favorit). Subsequently, $4.00 \pm 0.1\ \text{g}$ ($0.01\ \text{mol}$) of NaOH was also weighed and dissolved in 50 ml of absolute ethanol in 250 ml Schott bottle under the same condition as the Zinc precursor. The NaOH solution was slowly drained dropwise from a burette into the ZnCl_2 solution, maintaining the temperature at 60°C with vigorous stirring for 60 minutes until a white precipitate was formed. The mixture was cooled at room temperature for 180 minutes before centrifuging with FLETA 5 Multi-Purpose Centrifuge at 4000 rpm for 30 minutes. The precipitate was filtered using $0.45\ \mu\text{m}$ Whatman filter membrane, washed twice with acetone and then with deionized water, dried at room temperature, and finally ground in a powdery form for characterization.

2.4. Sorbate preparation.

Stock solutions of both L-ZnO-NPs and C-ZnO-NPs were prepared by dissolving $1.00 \pm 0.1\ \text{g}$ each of the nanocrystalline powder of each sample in 10.0 ml of concentrated HNO_3 acid, sonicated using Ney ULTRASONIK (15 min; 20 KHz; 200 W/L) and a solution made up to 1000 mg/l using DW. Serial dilutions of 0.2-2.0 mg/l were prepared from the stock solution

and analyzed spectroscopically using Atomic Absorption Spectrometer (iCE 3000 Series AA, Thermo Scientific). Conductivity and pH of the solution were also determined by EUTECH COND 6⁺ and PHS-W Series Benchtop pH/mV Meter, respectively.

2.5. Characterization of sorbent and sorbate.

RCH and L-ZnO-NPs Infrared spectra were obtained in KBr disks from 400–4000 cm⁻¹ using Thermo Nicolet iS10 Fourier transform IR spectrometer. The specific surface areas were determined from the adsorption-desorption nitrogen isotherms using a Quantachrome, US Autosorb iQ, version 2.01 apparatus. Samples were degassed at 175 °C for 120 minutes prior to the analysis [45] in flowing N₂ gas. The surface area was computed by applying the Brunauer–Emmett–Teller (BET) technique from the linear part of the nitrogen adsorption isotherm. Morphology of the RCH and L-ZnO-NPs were evaluated using Field Emission Scanning Electron Microscopy, FESEM (Carl Zeiss GeminiSEM 500) with an acceleration voltage of 10.0 kV, with a chamber pressure of 40 Pa and a working distance of 11.6 mm. Also, Transmission Electron Microscopy analysis, TEM was carried out using TEM (JEOL 1230, Japan) with the sample loaded onto a Foamvar film Copper grid (FF300-Cu) before being observed. The elemental components of the samples were analyzed with Energy-dispersive X-ray Spectroscopy, EDX (JEOL 6390LA, Japan). L-ZnO-NPs were further characterized using X-ray Diffraction, XRD, (Panalytical X'Pert Pro MPD PW3040/60) for its crystal structure and crystallite size. Diffraction patterns from the XRD analysis in Figure 3 were obtained using X-ray diffractometer with Cu-K α radiation of 40 kV and 30 mA with a step size of 0.017°. Sample preparation for FE-SEM, EDX, and FT-IR were carried out using the method outlined by [46-47].

2.6. Batch adsorption study.

ZnO-NPs sorption from solution onto RCH was examined in a batch mode as a function of the sorbent mass, contact time, pH, initial sorbate concentration, and temperature. Each study utilized 50 ml of known concentration of the sorbate solutions (L-ZnO-NPs and C-ZnO-NPs) with 0.5 g of RCH added in a 250 ml covered Erlenmeyer flask at 30 \pm 0.5 °C, and the mixture stirred on an electric hotplate magnetic stirrer (Fisherbrand) at 150 min⁻¹ at a speed of 450 rpm. Aliquots of the samples were taken during stirring at preset time intervals and filtered using 0.45 μ m filter paper and analyzed spectroscopically using AAS. All experiments were conducted in duplicates and two controls (adsorbent + DW; and DW only) in order to estimate the amount of any Zn that might be present in the sorbent. The initial sorbate concentration in the test solution and the adsorbent dosage was varied to investigate their effect on the sorption kinetics. The pH impact was investigated over a pH range of 2-13, where adjustments were made using NaOH or HCl solution and a pH meter. The study also varied the temperature in a range of 298-343 K to determine the effect of the thermodynamic parameters. The quantity of sorption at time t, q_t (mg/g), was computed by employing the equation:

$$\text{Removal}(\%) = (C_o - C_e) / C_o \times 100 \quad (1)$$

$$q_e = (C_o - C_e) \cdot V / W \quad (2)$$

Where, C_o and C_e (mg/L) represent the sorbate ions concentrations at initial, and equilibrium contact time, respectively, V represents the solution volume (L) and W is the mass of adsorbent used (g) and q_e is the amount of sorbate adsorbed at equilibrium (mg/g).

2.7. Kinetic study.

Sorption kinetics of both L-ZnO-NPs and C-ZnO-NPs onto RCH were determined using pseudo-first-order, pseudo-second-order, and intra-particle diffusion models were used. The equations for pseudo-first-order (Equ. 3), pseudo-second-order (Equ. 4) and intra-particle diffusion (Equ. 5) models are represented as follows;

$$\log(q_e - q_t) = \log q_e - k_1 t / 2.303 \quad (3)$$

Where; k_1 (min^{-1}) - rate constant of the pseudo-first-order sorption, q_t (mg/g) - the amount of ZnO-NPs adsorbed by sorbent at time t (min) and q_e (mg/g) - the amount of ZnO-NPs adsorbed at equilibrium. The fairly linear plots of $\log(q_e - q_t)$ versus t confirm the applicability of the above equation for ZnO-NPs onto sorbent. The value of k_1 was calculated from the slope of this linear plot.

$$t/q_t = 1/k_2 q_e^2 + t/q_e \quad (4)$$

Where; k_2 (g/mg min^{-1}) is rate constant. k_2 and q_e can be obtained from the intercept and slope of plotting of t/q_t versus t .

$$q_t = k_{id} \sqrt{t} + I \quad (5)$$

Where, k_{id} is intra-particle diffusion rate constant ($\text{mg/g min}^{1/2}$), and I is the thickness of the boundary layer (mg/g).

A linear relationship of Weber-Morris plot of q_t versus \sqrt{t} satisfies the sorption process to be controlled by intra-particle diffusion only. Multi-linear plots signify more than two steps influencing the sorption process.

2.8. Equilibrium study.

The sorption equilibrium data obtained was analyzed using three isotherm models; Langmuir, Freundlich, and Temkin isotherms. Langmuir isotherm model assumes that a finite number of active sites are distributed homogeneously over the surface of the sorbent with the same affinity for adsorption. The equation is expressed as;

$$1/q_e = [1/Q_o K] 1/C_e + 1/Q_o \quad (6)$$

Where, C_e – equilibrium concentration, mg/g, q_e – amount absorbed at equilibrium, mg/g, Q_o , and K – Langmuir constants relating to adsorption capacity and energy of adsorption, which was determined from the slope and intercept of the linear plot of $1/q_e$ Vs. $1/C_e$. The essential features of a Langmuir isotherm can be expressed in terms of a dimensionless constant separation factor R_L that is used to predict the favorability or non-favorability of the sorption process. The separation factor, R_L is defined by the equation:

$$R_L = 1/1 + KC_o \quad (7)$$

Where, C_o – sorbate concentration, mg/l, K – Langmuir adsorption equilibrium constant, L/g. The isotherm is unfavorable when R_L is greater than 1, the isotherm is linear when R_L is equal to 1, the isotherm is favorable when R_L is greater than 0 but less than 1, and the isotherm is irreversible when R_L is equal to 0.

Freundlich isotherm model assumes that, as the sorbate concentration increases, its concentration on the sorbent surface also increases, and correspondingly, the sorption energy exponentially decreases on completion of the sorption centers of the adsorbent. The equation relating to this model is:

$$\log q_e = \log K_f + \frac{1}{n} \log C_e \quad (8)$$

Where, q_e – amount adsorbed at equilibrium, mg/g, C_e – equilibrium concentration, mg/l, K_f and n – Freundlich model constants. These constants can be obtained from the slope and intercept of the plot of $\log q_e$ against $\log C_e$.

Temkin isotherm also assumes that the fall in the heat of sorption is linear rather than logarithmic, as implied in the Freundlich equation. The isotherm model relates the equation:

$$q_e = B_T \ln A_T + B_T \ln C_e \quad (9)$$

Where, $B_T = (RT/b_T)$, q_e – amounts adsorbed at the equilibrium concentration, mg/g, C_e – amounts adsorbed at the equilibrium concentration, mg/l, T – absolute temperature, K, R – universal gas constant, 8.314 J/(mol·K). The constant b_T is related to the heat of adsorption.

2.9. Thermodynamic study.

The thermodynamic concept assumes that in an isolated system, energy cannot be gained or lost, and the entropy change is the only driving force. In this study, both energy and entropy factors were considered to determine which process will occur spontaneously. Thermodynamic variables (ΔG° , ΔH° and $T\Delta S^\circ$) were determined using the equation;

$$\Delta G^\circ = -RT \ln K_c \quad (10)$$

$$K_c = q_e / C_e \quad (11)$$

$$\Delta G^\circ = \Delta H^\circ - T \Delta S^\circ \quad (12)$$

$$\ln K_c = -\Delta G^\circ / RT = \Delta S^\circ / R - \Delta H^\circ / RT \quad (13)$$

Where, R represents gas constant (8.314 J mol⁻¹K⁻¹), T represents temperature (K), ΔG° represent Gibbs free energy change, ΔH° represent enthalpy change, ΔS° is entropy change, and K_c is the distribution coefficient, q_e and C_e represent the equilibrium ZnO-NPs concentration on RCH (mg/g) and in the solution (mg/l) respectively.

ΔH° and ΔS° are determined from the slope and intercept of a linear vant' Hoff plot of $\ln (K_c)$ versus $1/T$.

3. Results and Discussion

3.1. Physico-chemical parameters.

Table 1. Physico-chemical characteristics of RCH and C-ZnO-NPs.

Sample	Characteristics	Value	Methodology
RCH	Bulk density (gcm ⁻³)	0.43 ±1.07	International Science Congress Association (ISCA)
	Particle density (gcm ⁻³)	0.61 ±1.92	Pycnometric method
	Moisture content (wt.%)	10.05 ±1.25	ASTM 2867-99
	Ash content (wt.%)	5.85 ±0.18	ASTM D2866-94
	% Extractives (wt.%)	9.89 ±1.19	ASTM D 1105-56
	α-Cellulose (wt.%)	44.31 ±0.88	ASTM D 1103-55T
	Lignin (wt.%)	42.58 ±0.53	ASTM D 1106-56
C-ZnO-NPs	Particle size	< 50 nm	
	BET	> 97%	
	Surface area	> 10.8 m ² /g	
	Density	> 5.61 g/ml	
	Dopant	6% Al	

3.2. Characterization.

3.2.1. XRD analysis.

Figure 2 shows the XRD pattern of L-ZnO-NPs prepared via solvothermal technique. The peaks observed at 2θ around 31.8, 34.7, 36.4, 47.8, 56.8, 63.0 and 68.0 corresponds to the

reflection from (010), (002), (011), (012), (110), (013), and (112) and are indexed to planes of hexagonal wurtzite structure of ZnO with ICSD Number (ICSD: 98000-9346) and PDF Number (Experimental and calculated powder diffraction data) of 36-1451 and 01-074-0534 respectively. The broadened patterns depict the nanosize of the ZnO crystals [44,48-49]. The XRD diffraction patterns of the synthesized NPs were identified as being 100 % pure ZnO with the average crystallite size calculated using Scherer's formula [50];

$$D = \frac{K\lambda}{\beta \cos \theta} \quad (14)$$

$$\beta = \sqrt{\beta^2 FWHM - \beta_0^2} \quad (15)$$

Where, K is shape factor = 0.89, β (FWHM) is the full-width half maximum of the diffraction peak, and β_0 is the correction factor for instrumental broadening ($0.07^\circ 2\theta$).

The mean crystallite size of the sample was found to be 14.7 ± 2.3 nm, which was similar to a study by [45] but with a flake-like morphology.

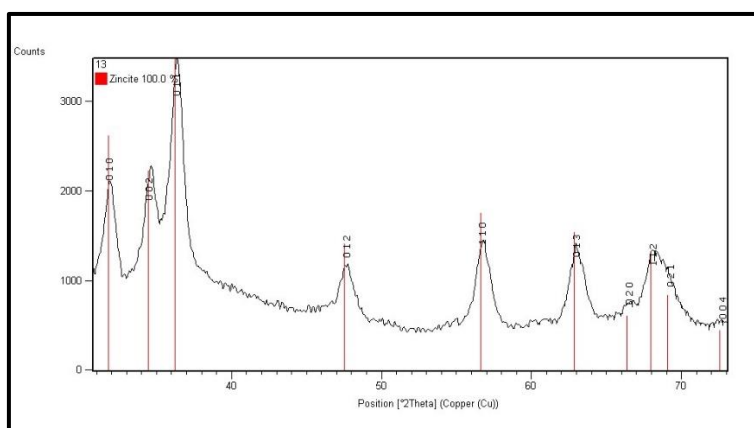


Figure 2. XRD diffractogram of L-ZnO-NPs synthesized using ZnCl_2 and NaOH.

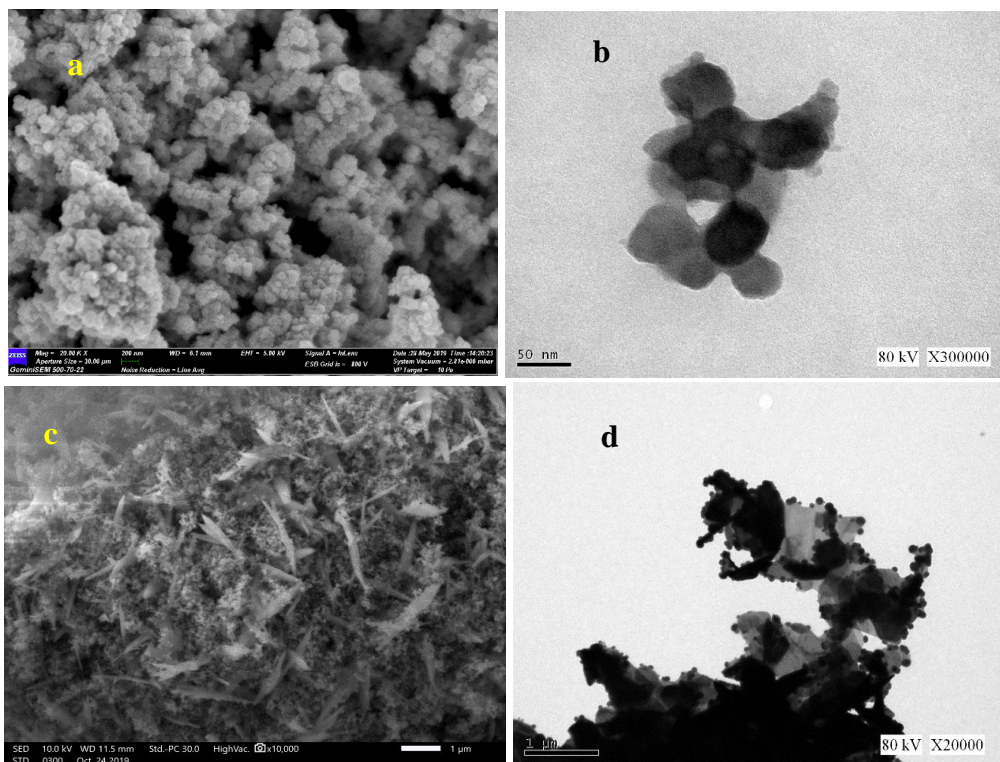


Figure 3. (a) FESEM (b) TEM images of L-ZnO-NPs (c) FESEM (d) TEM images of C-ZnO-NPs.

3.2.2. FESEM and TEM analysis.

The FESEM and TEM images of L-ZnO-NPs are represented in Figure 3 (a & b), respectively. The morphology of the synthesized sample (L-ZnO-NPs) revealed spherical shaped structures with agglomeration/aggregation of the particles. The average particle size recorded by the FESEM and TEM is 36.0 nm and 24.0 nm, respectively. Similar morphology was obtained when zinc acetate as a precursor in Triethanolamine (TEA) and Ethylene Glycol was used in a solvothermal method [51-52].

With respect to the adsorbent used for the studies, the SEM micrograph reveals significant changes in the surface morphology of the sorbent both before and after the adsorption process. The rough and heterogeneous surface nature of RCH before adsorption (Fig. 4a) predicts a high probability of active sites for the attachment of the sorbate ions [53]. The uptake of ZnO NPs onto RCH (Fig. 4b) reveals a change in morphology of the sorbent's surface been smooth.

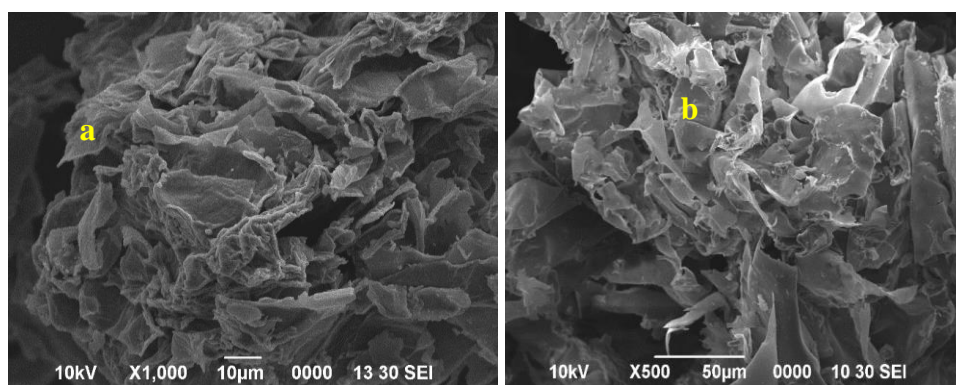


Figure 4. SEM micrograph of (a) RCH before adsorption (b) RCH after adsorption studies.

3.2.3. BET analysis.

The BET surface area of RCH determined from the isotherm plot, as shown in Fig 5, was found to be 2.60 m²/g with average pore size and volume of 6.53e+01 Å and 8.45e-03 cm³/g, respectively. The adsorption isotherm for this sample corresponds to Type IV based on the IUPAC classification in determining the surface area of samples reported by [54]. This type reveals the presence of a mesoporous surface structure often correlated to the presence of slit-shaped mesopores [55]. Though the surface area tends to be small, the multiple functional groups from the FTIR characterization of the sorbent enhanced the adsorption capacity.

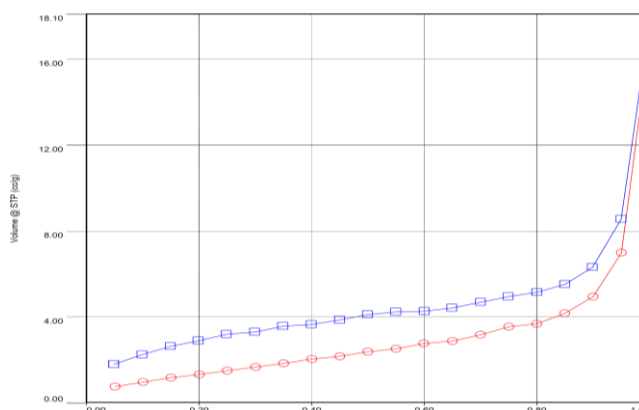


Figure 5. N₂ adsorption- desorption isotherms of RCH sorbent.

3.2.4. EDX analysis.

EDX spectra of the samples (L-ZnO-NPs and RCH) displayed in Figure 6 (a & b) detailed the elemental compositions of each sample. From the analysis, the samples appear to be pure according to their elemental compositions.

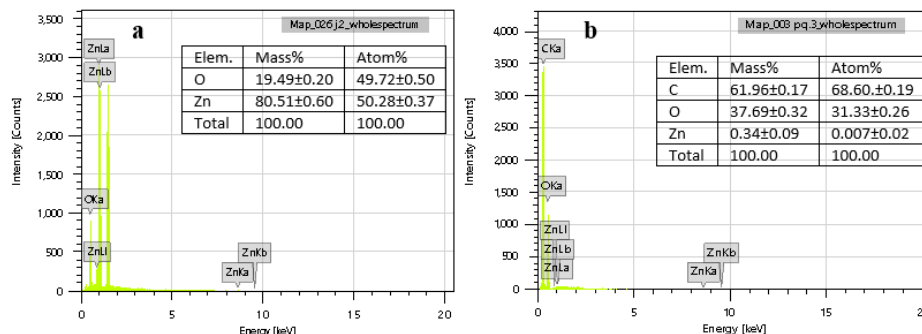


Figure 6. EDX spectra of (a) L-ZnO-NPs (b) RCH.

3.2.5. FT-IR analysis.

The infrared spectra of L-ZnO NPs and RCH used in this study are shown in Figure 7 (a & b). The characteristic band of wurtzite ZnO in L-ZnO-NPs sample occurred at a peak height of 580.02 cm^{-1} . This agrees with a study by [56-57] who reported the characteristic band for ZnO stretching mode in the range of $420\text{--}660\text{ cm}^{-1}$ when zinc nitrate hexahydrate and polyethylene glycol was used in a ZnO synthesis using the microwave-assisted solvothermal technique. The characteristic broad bands observed at 3124.53 cm^{-1} and 1543.40 cm^{-1} (in the case of L-ZnO-NPs) correspond to O-H stretching and bending of the hydroxyl group. The intense sharp peak at 1400.97 cm^{-1} could be attributed to $\text{C}-\text{H}$ bending in an alkane.

However, IR spectrum of RCH (Fig 7b) reveals a broad peak positioned at 3336 cm^{-1} to be attributed to O-H stretching vibration due to the intermolecular hydrogen bonding of alcohols, phenols, and carboxylic acids verifying the presence of hydroxyl functional group on the sorbent surface [58].

The peak located at 2359 cm^{-1} could also be associated with the presence of $\text{C}-\text{H}$ stretching in alkanes. The spectra also showed major peaks at 1743 cm^{-1} , 1512 cm^{-1} , 1449 cm^{-1} , and 1222 cm^{-1} to be an indication of the presence of $\text{C}=\text{O}$, $\text{C}=\text{C}$ stretching vibration of cyclic alkene, $\text{N}=\text{O}$ bending in nitro groups and $\text{C}-\text{N}$ in amine compound respectively [31,59].

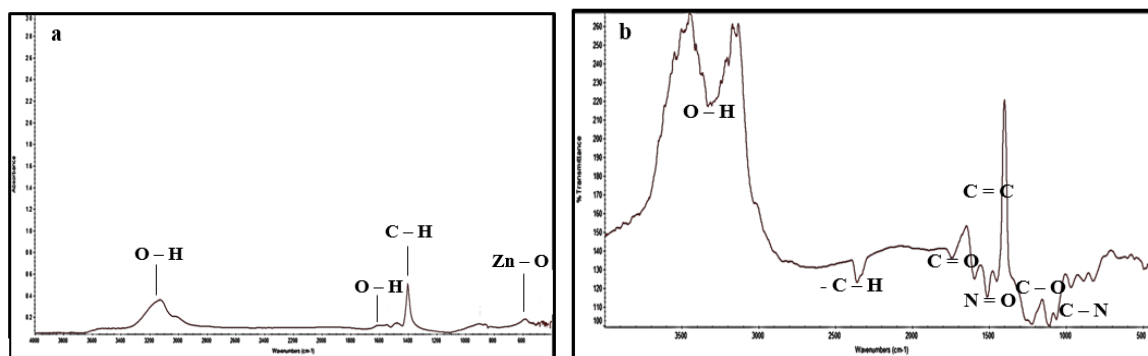


Figure 7. FT-IR spectrum of (a) L-ZnO-NPs and (b) RCH.

3.3. Batch adsorption studies.

3.3.1. Effect of adsorption parameters.

The effect of sorbent mass, pH, and initial sorbate concentrations were varied to determine the percentage removal and sorption capacity of both L-ZnO-NPs and C-ZnO-NPs by RCH, which are illustrated in Figure 8.

The sorbent mass was varied from 0.5 g to 2.5 g at a constant pH of 6.0, stirred at 450 rpm for 60 min. The concentration of the sorbate solutions was kept at 2.03 mg/l and 1.72 mg/l for L-ZnO-NPs and C-ZnO-NPs, respectively. According to Figure 8a, the percentage removal of both ZnO-NPs increased with increasing sorbent mass until equilibrium was attained at 2.0 g with a maximum percentage removal of 88.56% and 90.05% for L-ZnO-NPs and C-ZnO-NPs respectively. This significant increase in percentage removal was due to the increased active sites as well as greater surface availability for the uptake of the sorbate ions [60-61]. The percentage of adsorption suddenly decreased slightly for both sorbate solutions (88.12% and 88.90%) as the sorbent mass increased to 2.5 g. On the contrary, the sorption efficiency (q_e) was inversely proportional to the sorbent mass as the lowest efficiency (0.04 mg/g and 0.03 mg/g) for L-ZnO and C-ZnO NPs respectively was recorded at the maximum sorbent mass of 2.5 g. This effect may be attributed to the difficulty in the mass transfer, as well as the unsaturation and screening effect of the surface area of the sorbent [62-64].

The pH of the sorbate solution was varied between 2-13 at an initial concentration of 2.03 mg/l and 1.72 mg/l for L-ZnO-NPs and C-ZnO-NPs, respectively. The sorbent mass (0.5 g), stirring rate (450 rpm), and time (60 min) were all kept constant. The pH changes of the medium usually influence the surface reactivity of the sorbent through the uptake of the sorbate ions through hydrogen bonding and/or ion exchange mechanisms [65-66]. According to Figure 8b, the highest and lowest percentage of removal was observed at a pH of 8 and 2 for both sorbate solutions. At lower pH, active sites are protonated, leading to high electrostatic repulsion between the sorbate ions and the active sites resulting in lower uptake. However, as pH increases to the optimum level of 8, hydrogen ions (H^+) decrease, which enables the sorbate ions to bind to the increasing negative surface charge of the sorbent [34,61]. Precipitation of metal hydroxide species [$Zn(OH)_2$] occurs beyond the optimum pH, which competes with the sorbate ions for an active site for attachments [67]. Besides, agglomeration/aggregation of the L-ZnO-NPs also contributed to the difference in the uptake of the two sorbate ions.

The variation in % sorbate removal with contact time given different initial concentrations ranging from 0.46-1.45 mg/l and 0.50-1.74 mg/l for L-ZnO and C-ZnO NPs sorbate solutions respectively is shown in Figure 8 (c & d). The sorbent mass (0.5 g), stirring rate (450 rpm), and pH (6.0) were all kept constant. The percentage removal of sorbate ions remarkably increased for the first 80 minutes before showing a decreasing trend for all the concentrations in both sorbate solutions. The average % removal increased from 83.7% to 88.0% (0.04-0.13 mg/g) for L-ZnO-NPs and 85.6% to 88.8% (0.04-0.16 mg/g) for C-ZnO-NPs as initial concentrations of the sorbate solution increases. The increase in adsorption efficiency may likely be attributed to the driving force of mass transfer or diffusion processes from the bulk to the surface [25,68]. However, beyond the equilibrium point, the adsorption sites got exhausted, leading to a decrease in the efficiency of RCH [69]. Adsorption at lower and higher concentrations tends to be slightly proportional according to the data set since at higher concentrations. Active sites tend to be slightly saturated as compared to lower concentrations.

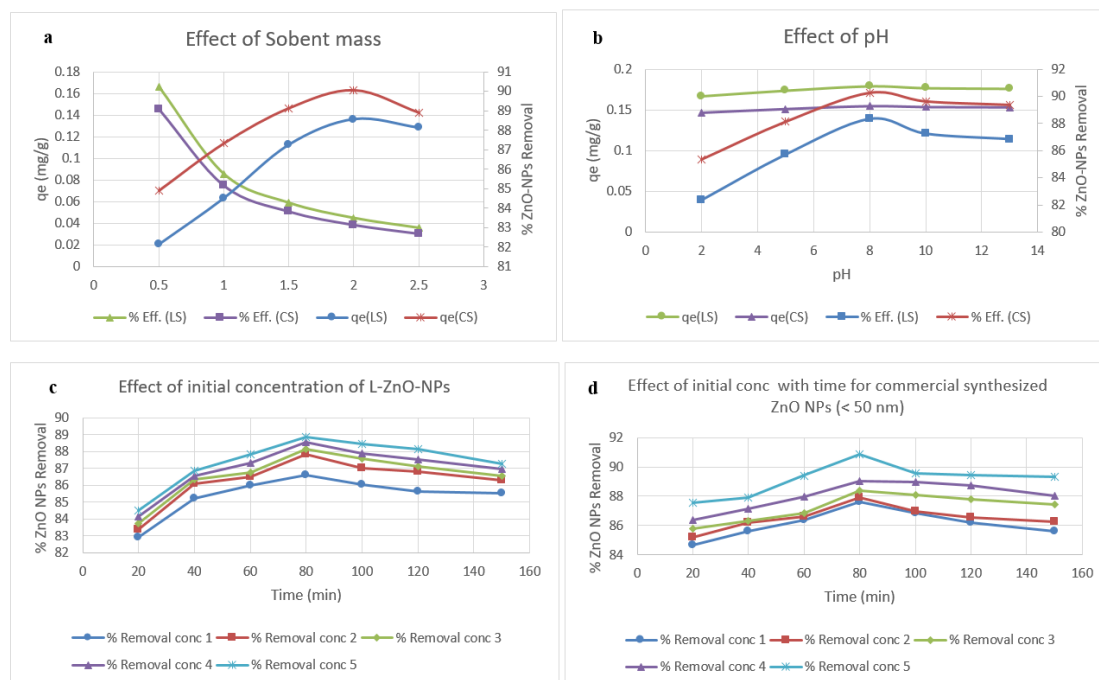


Figure 8. Effect of (a) sorbent mass (b) pH on L-ZnO and C-ZnO NPs sorption on RCH (c & d) initial concentration (L-ZnO & C-ZnO-NPs).

3.4. Isothermal studies.

Equilibrium data analysis for the sorption of sorbate solutions (L-ZnO & C-ZnO-NPs) onto RCH was carried out using three isotherm models shown in Table 2.

Table 2. Langmuir, Freundlich and Temkin parameters for L-ZnO-NPs and C-ZnO-NPs uptake,

Parameters	L-ZnO-NPs	C-ZnO-NPs
Langmuir isotherm ($\frac{1}{q_e} = \left[\frac{1}{Q_0 K} \right] \frac{1}{C_e} + \frac{1}{Q_0}$)		
Q_0 [mg/g]	0.797	0.710
K , [L/g]	0.430	0.396
R^2	1.00	0.996
Freundlich isotherm ($\log q_e = \log K_f + \frac{1}{n} \log C_e$)		
K_f , [L/g]	1.084	0.896
n	1.166	1.246
R^2	0.999	0.986
Temkin isotherm ($q_e = B_T \ln A_T + B_T \ln C_e$)		
A_T , [L/g]	0.764	0.663
B_T	11.40	6.658
b_T	220.90	378.34
R^2	0.958	0.799

From Table 2, Langmuir and Freundlich's models fit best for L-ZnO-NPs, whereas, in the case of C-ZnO-NPs, Langmuir model was considered to be the best fit based on their correlation coefficients (R^2). With reference to the Langmuir isotherm model, the sorption of ZnO-NPs onto RCH was monolayer occurring on a homogenous surface. The theoretical sorption capacity (Q_0) recorded for this model was 0.797 mg/g and 0.710 mg/g for L-ZnO-NPs and C-ZnO-NPs, respectively. This presupposes that the potential for RCH to remove L-ZnO-NPs from aqueous solution was higher than L-ZnO-NPs. However, Langmuir isotherm best fitted for a study by [70] with a sorption capacity ranged between 1.0×10^{-4} to 3.9×10^{-4} mg/g for the removal of Cu, Cd, Fe, Cr, and Pb ions respectively from aqueous solution using

coconut husk. Meanwhile, the calculated separation factor (R_L) illustrated in Table 3 for this isotherm model for both sorbates was between 0 and 1, indicating favorable sorption.

Table 3. Separation factor (R_L) for L-ZnO-NPs and C-ZnO-NPs uptake.

[C ₀] L-ZnO-NPs (mg/l)	R_L L-ZnO-NPs	[C ₀] C-ZnO-NPs (mg/l)	R_L C-ZnO-NPs
0.462	0.846	0.501	0.835
0.884	0.741	0.844	0.750
1.045	0.708	1.247	0.670
1.259	0.668	1.523	0.624
1.451	0.635	1.736	0.593

The n-value from the Freundlich isotherm model demonstrates the degree of non-linear mechanism between the sorbate solution and the sorbent. When $n = 1$, it describes the linearity of the process. If $n < 1$, suggests that the sorption process is unfavorable, and if $n > 1$, the sorption process is considered to be favorable [71-72]. From the current study, the value of n for the two sorbate solutions (1.166 & 1.246) is greater than unity suggesting the favourability of the process.

Temkin model assumes chemical sorption is favorable when a linear decrease occurs in the sorption energy between the interactions between the sorbent and sorbate [73]. The correlation coefficients of 0.958 and 0.799 recorded for the two sorbate solutions in this study do not fit well for the sorption process.

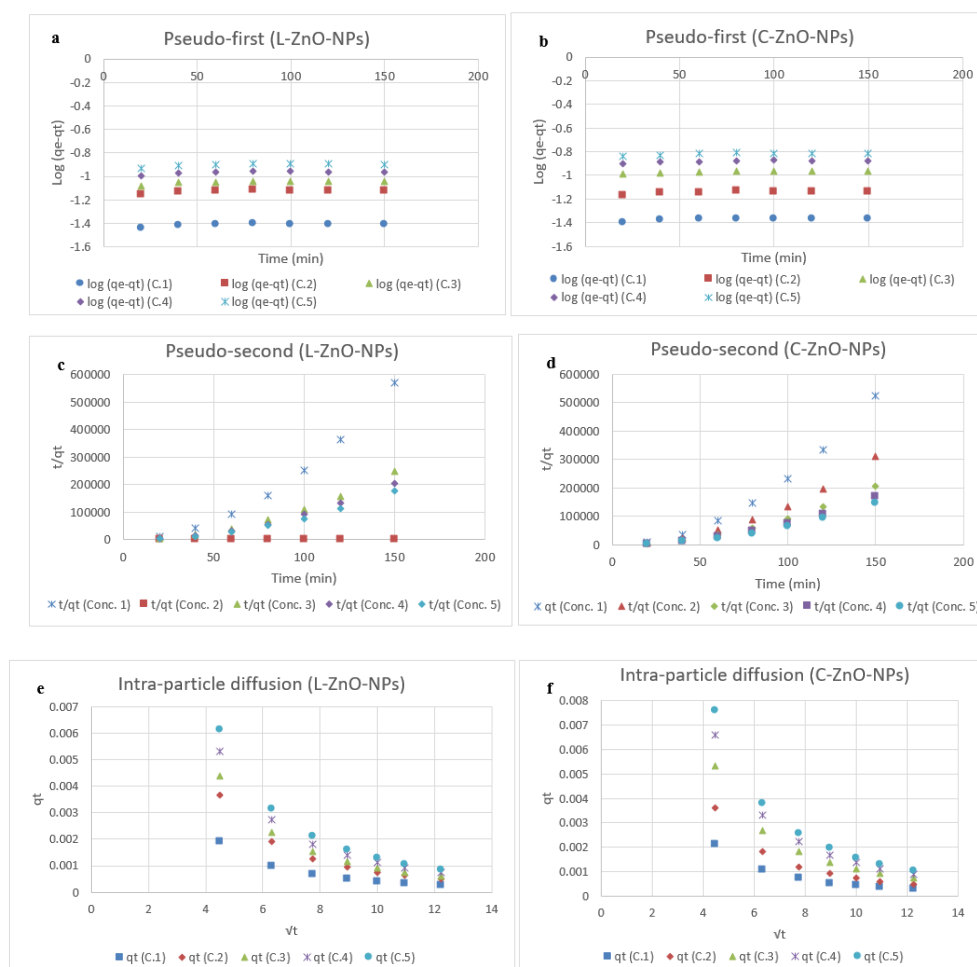


Figure 9. (a) Pseudo-first [L-ZnO-NPs] (b) Pseudo-first [C-ZnO-NPs] (c) Pseudo-second [L-ZnO-NPs] (d) Pseudo-second [C-ZnO-NPs] (e) Intra-particle diffusion [L-ZnO-NPs] (f) Intra-particle diffusion [C-ZnO-NPs] kinetic plots for adsorption of ZnO-NPs onto RCH.

Table 4. Adsorption kinetic parameters for L-ZnO-NPs and C-ZnO-NPs.

Initial conc, C ₀ [mg/l]	Pseudo-first order ($\log(q_{\theta} - q_t) = \log q_{\theta} - \frac{k_1 t}{2.303}$)				Pseudo-second order ($\frac{t}{q_t} = \frac{1}{k_2 q_{\theta}^2} + \frac{t}{q_{\theta}}$)			Intra-particle diffusion ($q_t = k_{id}\sqrt{t} + I$)		
	q _{e,theo.} (mg/g)	k ₁ (min ⁻¹)	R ²	q _{e,exp} (mg/g)	q _{e,theo.} (mg/g)	k ₂ (g/mg.min)	R ²	K _{id} (mg/(g min ^{1/2}))	I (mg/g)	R ²
L-ZnO-NP	0.037	4.61×10 ⁻⁴	0.511	0.039	2.34×10 ⁻⁴	7.40×10 ⁻⁶	0.947	2.00×10 ⁻⁴	2.40×10 ⁻³	0.837
	0.072	4.61×10 ⁻⁴	0.514	0.076	10 ⁻⁴	0.383	0.999	10 ⁻⁴	10 ⁻³	0.838
	0.462	0.085	4.61×10 ⁻⁴	0.516	0.090	1.70×10 ⁻⁵	0.946	4.00×10 ⁻⁴	4.70×10 ⁻³	0.838
	0.884	0.103	10 ⁻⁴	0.517	0.110	2.05×10 ⁻⁵	0.946	10 ⁻⁴	10 ⁻³	0.837
	1.045	0.119	4.61×10 ⁻⁴	0.523	0.127	2.38×10 ⁻⁵	0.946	4.00×10 ⁻⁴	5.50×10 ⁻³	0.837
	1.259	10 ⁻⁴			6.51×10 ⁻⁴			10 ⁻⁴	10 ⁻³	
	1.451	4.61×10 ⁻⁴			7.54×10 ⁻⁴			5.00×10 ⁻⁴	6.70×10 ⁻³	
C-ZnO-NP	0.041	4.61×10 ⁻⁴	0.466	0.043	2.55×10 ⁻⁴	8.02×10 ⁻⁶	0.946	2.00×10 ⁻⁴	2.70×10 ⁻³	0.832
	0.070	10 ⁻⁴	0.507	0.073	10 ⁻⁴	1.36×10 ⁻⁵	0.947	10 ⁻⁴	10 ⁻³	0.832
	0.501	0.103	4.61×10 ⁻⁴	0.673	0.108	2.05×10 ⁻⁵	0.947	4.00×10 ⁻⁴	4.50×10 ⁻³	0.829
	0.844	0.127	10 ⁻⁴	0.633	0.134	2.52×10 ⁻⁵	0.947	10 ⁻⁴	10 ⁻³	0.830
	1.247	0.147	4.61×10 ⁻⁴	0.583	0.155	2.91×10 ⁻⁵	0.947	5.00×10 ⁻⁴	6.70×10 ⁻³	0.830
	1.523	10 ⁻⁴			7.97×10 ⁻⁴			10 ⁻⁴	10 ⁻³	
	1.736	4.61×10 ⁻⁴			9.20×10 ⁻⁴			8.00×10 ⁻⁴	9.60×10 ⁻³	

Table 5. Thermodynamic studies of L-ZnO-NPs and C-ZnO-NPs adsorption onto RCH.

C ₀ (mg/l)	T (K)	ΔG° (kJmol ⁻¹)	ΔS° (JK ⁻¹ mol ⁻¹)	ΔH° (kJmol ⁻¹)	R ²	C ₀ (mg/l)	T (K)	ΔG° (kJmol ⁻¹)	ΔS° (JK ⁻¹ mol ⁻¹)	ΔH° (kJmol ⁻¹)	R ²
L-ZnO-NPs			7.82	-3893.78	0.564	C-ZnO-NPs			7.88	-3572.86	0.526
0.462	298	1734.67				0.622	298	1386.69			
	303	1550.58					303	1189.06			
	313	1298.94					313	1025.81			
	323	1097.98					323	712.06			
	333	1281.88					333	982.89			
343	1443.73	343				1074.88					
0.884	298	1388.04	2.16	-1816.03	0.302	0.837	298	1212.03	10.56	-4257.52	0.602
	303	1059.45					303	1102.69			
	313	1003.40					313	943.76			
	323	1002.68					323	492.96			
	333	1109.32					333	738.85			
343	1210.55	343	856.50								
1.045	298	1333.27	3.13	-2079.50	0.416	1.215	298	1167.37	13.31	-5034.79	0.703
	303	1051.24					303	1064.56			
	313	966.38					313	818.21			
	323	964.57					323	425.79			
	333	1035.31					333	570.03			
343	1134.76	343	701.01								
1.259	298	1293.51	4.90	-2568.11	0.495	1.474	298	1095.12	13.36	-4964.37	0.703
	303	1021.12					303	978.83			
	313	903.99					313	704.72			
	323	841.37					323	351.88			
	333	941.45					333	501.12			
343	1034.18	343	606.17								
1.451	298	1186.03	4.25	-2261.57	0.381	1.621	298	1016.74	13.63	-4945.92	0.644
	303	929.71					303	885.88			
	313	785.51					313	550.01			
	323	701.37					323	257.62			
	333	864.68					333	354.33			
343	967.86	343	531.93								

3.5. Kinetic studies.

Three kinetic models, thus pseudo-first-order, pseudo-second-order, and intra-particle diffusion models, were applied to evaluate the controlling mechanism of both sorbate solutions (L-ZnO-NPs and C-ZnO-NPs) onto RCH. The calculated rate constants and their correlation

coefficients are illustrated in Table 4 with Figure 9 graphically show the plots of time with their initial sorbate concentrations.

Pseudo-second order was the appropriate model that describes the process based on their correlation coefficient (R^2) values, which are closer to unity despite their estimated experimental q_e values, which are far below the theoretical q_e values. However, experimental q_e values of the pseudo-first-order model were quite close to the experimental values shown in Table 4. Although the pseudo-first-order rate showed a poor correlation coefficient of 0.52, the intra-particle diffusion model records a slightly higher correlation coefficient (0.84) than pseudo-first-order but lower than pseudo-second-order (0.95). This presupposes that intra-particle diffusion cannot solely describe the sorption of ZnO-NPs onto RCH as the plotted lines do not pass through the origin. The plot displayed a multi-linear nature (Fig 9 e & f) for the experimental data confirming the sorption mechanism to be in two steps [74]. The two steps of the curve might be due to the boundary layer diffusion effect and intra-particle diffusion effect [75]. The thickness of the boundary layer expressed by the intercept (I) is lower in this study indicating minimal boundary layer effect. The calculated values of intra-particle diffusion rate constant, K_{id} decreases with increasing sorbate concentrations, as illustrated in Table 4.

3.6. Thermodynamic studies.

The removal of ZnO-NPs by RCH as sorbent was determined at temperature ranges of 298-343 K for five initial sorbate concentrations and the thermodynamic variables [Gibbs free energy (ΔG°), enthalpy change (ΔH°) and entropy change (ΔS°)] as well as their calculated correlation coefficients are illustrated in Table 5.

The positive values of ΔG° obtained for both sorbates at the different temperatures reveal a non-spontaneous sorption process, which requires an external source of energy. On the other hand, positive values recorded for ΔS° demonstrates the occurrence of a degree of freedom at the RCH-ZnO-NPs solution interface during the sorption process. It also suggests an increase in the randomness and affinity of the sorbate solution towards RCH [29]. Meanwhile, the negative values recorded for ΔH° confirms the exothermic nature of the sorption process as the high ΔH° values suggests a chemical sorption process.

4. Conclusions

Zinc oxide NPs were successfully synthesized through a solvothermal method with spherical shaped morphology. Characterization by XRD, FE-SEM, TEM revealed the crystallite and average particle size to be 14.7 nm, 36.0 nm, and 24.0 nm, respectively. The surface area of the sorbent (RCH) determined through BET analysis revealed a size of 2.60 m^2/g with a porous surface nature. FT-IR confirmed functional groups such as hydroxyl, carboxyl, and nitro groups as present on the sorbent. The morphology of the sorbate particles in solution been agglomerated slightly influenced the sorption capacity of the RCH as the uptake of L-ZnO-NPs onto RCH was lesser as compared to C-ZnO-NPs. The optimum sorbent mass to remove 88% and 90% of L-ZnO-NPs and C-ZnO-NPs, respectively, is 2.0 g. Adsorption efficiency increased with an increase in initial sorbate concentration to the 80th minute when maximum removal was obtained (0.13 mg/g and 0.16 mg/g for L-and C-ZnO-NPs) at an optimum pH of 8. Langmuir and Freundlich isotherm models fitted best for L-ZnO-NPs with maximum sorption capacity of 0.78 mg/g, whereas the Langmuir model also fitted well for C-ZnO-NPs with maximum sorption capacity of 0.71 mg/g. The sorption process was identified to be exothermic with non-spontaneous and random sorption processes, which was

best described by the pseudo-second-order model. However, the lignocellulose material used in this study could help alleviate the pollution effect of water bodies with these nanoparticles that are very difficult to eliminate due to their sizes.

Funding

This research received no external funding.

Acknowledgments

The authors acknowledge the contribution of colleagues from the Faculty of Resource Science and Technology (FRST) Geochemistry Laboratory and Analytical Laboratory, Universiti Malaysia Sarawak, and Departments of Science, Kibi Presbyterian College of Education, Kibi, Eastern Region, Ghana.

Conflicts of Interest

The authors declare that they have no competing interests regarding the publication of this manuscript. Also, issues of plagiarism, data fabrication and or falsification, double publication, and or submission have been completely observed by the authors. EK Droepenu and EA Asare undertook the collection of the coconut husk. EK Droepenu, AE Asare, and AO Gyampoh designed the research. EK Droepenu carried out the laboratory work. EK Droepenu, AE Asare, AO Gyampo, E Kumi-Arhin, SB Dampare, and DK Adotey conducted the review and editing. Finally, all authors have read and approved the manuscript for publication.

References

1. Broomfield, M.; Hansen, S.F.; Pelsy, F. Support for 3rd regulatory review on nanomaterials-environmental legislation. Project Report. *European Commission* **2016**, <https://doi.org/10.2779/49879>.
2. Sarmah, K.; Pratihari, S. Synthesis, characterization and photocatalytic application of iron oxalate capped Fe, Fe-Cu, Fe-Co, and Fe-Mn oxide nanomaterial. *ACS Sustain. Chem. Eng.* **2017**, *5*, 310-324, <https://doi.org/10.1021/acssuschemeng.6b01673>.
3. Chen, H.; Zhao, L.; Wang, G.; Fang, W. Direct growth of ZnO nanorods on biogenic hierarchical rice husk SiO₂ and their application to dye degradation. *Clean Techn. Environ. Policy* **2017**, *19*, 1335-1345, <https://doi.org/10.1007/s10098-017-1332-2>.
4. Zhao, Y.; Yu, N.; Dong, X.; Yan, H. Large area growth of ZnO Nanorods arrays on the stainless steel grid by aqueous solutions. *Materials Research Innovations* **2017**, *21*, 447-450, <https://doi.org/10.1080/14328917.2016.1265261>.
5. Husham, M.; Nizar, M.H.; Paiman, S.; Abuelsamen, A.A.; Farhat, O.F.; Al-Dulaimi, A.A. Synthesis of ZnO nanorods by microwave-assisted chemical-bath deposition for highly sensitive self-powered UV detection application. *Sensor Act A* **2017**, *263*, 166-173, <https://doi.org/10.1016/j.sna.2017.05.041>.
6. Jeem, M.; Zhang, L.; Ishioka, J.; Shibayama, T.; Iwasaki, T.; Kato, T.; Watanabe, S. Tuning optoelectrical properties of ZnO nanorods with excitonic defects via submerged illumination. *Nano Lett.* **2017**, *17*, 2088-2093, <https://doi.org/10.1021/acs.nanolett.7b00324>.
7. Das, P.; Sarmah, K.; Hussain, N.; Pratihari, S.; Das, S.; Bhattacharyya, P.; Patil, S.A.; Kim, H.S.; Iqbal, M.; Khazie, A.; Bhattacharyya, S.S. Novel synthesis of an iron oxalate capped iron oxide nanomaterial; a unique soil conditioner and slow release eco-friendly source of iron sustenance in plants. *RSC Adv.* **2016**, *6*, 103012-103025, <https://doi.org/10.1039/C6RA18840K>.
8. Saranji, S.N. Controllable growth of ZnO nanorods via electrode position technique: towards UV photo-detection. *Journal of Physics D: Applied Physics* **2016**, *49*.
9. Gottschalk, F.; Sun, T.Y.; Nowack, B. Environmental concentrations of engineered nanomaterials: review of modeling and analytical studies. *Environ Pollut.* **2013**, *181*, 287-300, <https://doi.org/10.1016/j.envpol.2013.06.003>.
10. Wahab, R.; Khan, F.; Singh, R.B.; Kaushik, N.K.; Ahmad, J.; Siddiqui, M.A.; Saquib, Q.; Ali, B.A.; Khan, S.T.; Musarrat, J.; Al-Khedhairy, A.A. Utilization of photocatalytic ZnO nanoparticles for deactivation of safranin dye and their applications for statistical analysis. *Physica E: Low-dimensional Systems and Nanostructures* **2015**, *69*, 101-108, <https://doi.org/10.1016/j.physe.2015.01.005>.

11. Dwivedi, S.; Wahab, R.; Khan, F.; Mishra, Y.K.; Musarrat, J.; Al-Khedhairi, A.A. Reactive oxygen species mediated bacterial biofilm inhibition via zinc oxide nanoparticles and their statistical determination. *PLoS ONE* **2014**, *9*, 1-9, <https://doi.org/10.1371/journal.pone.0111289>.
12. Hölken, I. Complex shaped ZnO nano- and microstructure based polymer composites: mechanically stable and environmentally friendly coatings for potential antifouling applications. *Phys. Chem. Chem. Phys.* **2016**, *18*, 7114–7123, <https://doi.org/10.1039/C5CP07451G>.
13. Wahab, R.; Khan, F.; Mishra, Y.K.; Musarrat, J.; Al-Khedhairi, A.A. Antibacterial studies and statistical design set data of quasi zinc oxide nanostructures. *RSC Adv.* **2016a**, *6*, 32328–32339. <https://doi.org/10.1039/C6RA05297E>.
14. Wahab, R.; Kaushik, N.; Khan, F.; Kaushik, N.K.; Choi, E.H.; Musarrat, J.; Al-Khedhairi, A.A. Self-styled ZnO nanostructures promotes the cancer cell damage and suppresses the epithelial phenotype of glioblastoma. *Sci. Rep.* **2016b**, *6*, <https://doi.org/10.1038/srep19950>.
15. Wahab, R.; Siddiqui, M.A.; Saquib, Q.; Dwivedi, S.; Ahmad, J.; Musarrat, J.; Al-Khedhairi, A.A.; Shin, H.-S. ZnO nanoparticles induced oxidative stress and apoptosis in HepG2 and MCF-7 cancer cells and their antibacterial activity. *Colloids Surf. B Biointerfaces* **2014**, *117*, 267–276, <https://doi.org/10.1016/j.colsurfb.2014.02.038>.
16. Antoine, T.E.; Hadigal, S.R.; Yakoub, A.M.; Mishra, Y.K.; Bhattacharya, P.; Haddad, C.; Valyi-Nagy, T.; Adelung, R.; Prabhakar, B.S.; Shukla, D. Intravaginal zinc oxide tetrapod nanoparticles as novel immune-protective agents against genital herpes. *J. Immunol.* **2016**, *196*, 4566–4575, <https://doi.org/10.4049/jimmunol.1502373>.
17. Lee, K.M.; Lai, C.W.; Ngai, K.S.; Juan, J.C. Recent developments of zinc oxide based photocatalyst in water treatment technology: a review. *Water Research* **2016**, *88*, 428–448, <https://doi.org/10.1016/j.watres.2015.09.045>.
18. Sirelkhatim, A.; Mahmud, S.; Seeni, A.; Mohamad, N.H. Review on zinc oxide nanoparticles: antibacterial activity and toxicity mechanism. *Nano-Micro Letters* **2015**, *7*, 219–242, <https://doi.org/10.1007/s40820-015-0040-x>.
19. Jiang, J.; Pi, J.; Cai, J. The Advancing of Zinc Oxide Nanoparticles for Biomedical Applications. *Bioinorganic Chemistry and Applications* **2018**, 1-18, <https://doi.org/10.1155/2018/1062562>.
20. Qui, W.Z.; Yang, H.C.; Wan, L.S.; Xu, Z.K. Co-deposition of catechol/polyethyleneimine on porous membrane for efficient decolorization of dye water. *J. Matter. Chem. A* **2015**, *3*, 14438–14444, <https://doi.org/10.1039/C5TA02590G>.
21. Aljeboree, A.M.; Alshirifi, A.N.; Alkaim, A.F. Kinetics and equilibrium study for the adsorption of textile dye on coconut shell activated carbon. *Arab. J. Chem.* **2017**, *10*, 3381–3393, <https://doi.org/10.1016/j.arabjc.2014.01.020>.
22. Hao, J.; Li, C.; Hu, C.; Wu, K. Rapid, efficient and economic removal of organic dyes and heavy metals from wastewater by zinc-induced in-situ reduction and precipitation of graphene oxide. *J. Taiwan Inst. Chem. Eng.* **2018**, *88*, 137–145, <https://doi.org/10.1016/j.jtice.2018.03.045>.
23. Hadibarata, T.; Syafiuddin, A.; Al-Dhabaan, F.A.; Elshikh, M.S.; Rubiyatno. Biodegradation of Mordant orange-1 using newly isolated strain *Trichoderma harzianum* RY44 and its metabolite appraisal. *Bioproc. Biosyst. Eng.* **2018**, *41*, 621–632, <https://doi.org/10.1007/s00449-018-1897-0>.
24. El-Gohary, F.; Tawfik, A.; Mahmoud, U. Comparative study between chemical coagulation/precipitation (C/P) versus coagulation/dissolved air flotation (C/DAF) for pre-treatment of personal care products (PCPs) wastewater. *Desalination* **2010**, *252*, 106–112, <https://doi.org/10.1016/j.desal.2009.10.016>.
25. Wang, F.; Yang, W.; Cheng, P.; Zhang, S.; Zhang, S.; Jiao, W.; Sun, Y. Adsorption characteristics of cadmium onto microplastics from aqueous solutions. *Chemosphere* **2019**, *235*, 1073–1080, <https://doi.org/10.1016/j.chemosphere.2019.06.196>.
26. Al Farraj, D.A.; Hadibarata, T.; Yuniarto, A.; Syafiuddin, A.; Surtikanti, H.K.; Elshikh, M.S.; Al Khulaifi, M.M.; Al-Kufaidy, R. Characterization of pyrene and chrysene degradation by halophilic *Hortaea* sp. B15. *Bioprocess Biosystems Eng.* **2019**, *42*, 963–969, <https://doi.org/10.1007/s00449-019-02096-8>.
27. Kristanti, R.A.; Hadibarata, T.; Al Farraj, D.A.; Elshikh, M.S.; Alkufeydy, R.M. Biodegradation Mechanism of Phenanthrene by Halophilic *Hortaea* sp. B15. *Water, Air, & Soil Pollution* **2018**, *229*, <https://doi.org/10.1007/s11270-018-3969-9>.
28. Gisi, S.D.; Lofrano, G.; Grassi, M.; Notarnicola, M. Characteristics and adsorption capacities of low-cost sorbent for wastewater treatment: A review. *Sustain. Mat. Technol.* **2016**, *9*, 10–40, <https://doi.org/10.1016/j.susmat.2016.06.002>.
29. Jain, S.N.; Gogate, P.R. Adsorption removal of acid violet dye from wastewater using biosorbent obtained from NaOH and H₂SO₄ activation of fallen leaves of *Ficus racemosa*. *J. Mol. Liq.* **2017**, *243*, 132–143, <https://doi.org/10.1016/j.molliq.2017.08.009>.
30. Şentürk, İ.; Alzein, M. Adsorption of Acid Violet 17 onto Acid-Activated Pistachio Shell: Isotherm, Kinetic and Thermodynamic Studies. *Acta Chim. Slov.* **2020**, *67*, 1–15, <https://doi.org/10.17344/acs.2019.5195>.
31. Azani, N.F.S.M.; Chuin, C.T.H.; Abdullah, N.S.; Sharifuddin, S.S.; Hussin, M.H. Characterisation and Kinetic Studies on Activated Carbon Derived from Rubber Seed Shell for the Removal of Methylene Blue in Aqueous Solutions. *Journal of Physical Science* **2019**, *30*, 1–20, <https://doi.org/10.21315/jps2019.30.2.1>.

32. El Bardiji, N.; Ziat, K.; Saidi, M. Adsorption of copper from aqueous solution by Moroccan attapulgit: kinetic and thermodynamic studies. *Int. J. Adv. Res.* **2019**, *7*, 41-48, <https://doi.org/10.21474/IJAR01/9972>.
33. Aslam, M.; Rais, S.; Alam, M.; Pugazhendhi, A. Adsorption of Hg(II) from Aqueous Solution Using Adulsa (*Justicia adhatoda*) Leaves Powder: Kinetic and Equilibrium Studies. *Journal of Chemistry* **2013**, *2013*, 1-11, <https://doi.org/10.1155/2013/174807>.
34. Vassileva, P.S.; Radoykova, T.H.; Detcheva, A.K.; Avramova, I.A.; Aleksieva, K.I.; Nenkova, S.K.; Valchev, I.V.; Mehandjiev, D.R. Adsorption of Ag⁺ ions on hydrolysed lignocellulosic materials based on willow, paulownia, wheat straw and maize stalks. *Int. J. Environ. Sci. Technol.* **2016**, *13*, 1319–1328. <https://doi.org/10.1007/s13762-016-0970-y>.
35. Tran, H.D.; Vi, H.M.T.; Dang, H.T.T.; Narbaitz, R.M. Pollutant removal by *Canna Generalis* in tropical constructed wetlands for domestic wastewater treatment. *Global J. Environ. Sci. Manage.* **2019**, *5*, 331-344, <https://doi.org/10.22034/gjesm.2019.03.06>.
36. Aljeboree, A.M.; Alshirifi, A.N.; Alkaim, A.F. Kinetics and equilibrium study for the adsorption of textile dye on coconut shell activated carbon. *Arab. J. Chem.* **2017**, *10*, 3381–3393, <https://doi.org/10.1016/j.arabjc.2014.01.020>.
37. Taba, P.; Auliya, W.; Kasim, S.; Nafie, N.L.; Hala, Y. Adsorption of metal ion, Co(II) on *Eucheuma spinosum*. *J. Phys.: Conf. Ser.* **2019**, *1341*, 1-9, <https://doi.org/10.1088/1742-6596/1341/3/032034>.
38. Banerjee, M.; Basu, R.K.; Das, S.K. Cr(VI) adsorption by a green adsorbent walnut shell: adsorption studies, regeneration studies, scale-up design and economic feasibility. *Process Safety and Environment Protection* **2018**, *116*, 693-702, <https://doi.org/10.1016/j.psep.2018.03.037>.
39. Anuar, F.I.; Hadibarata, T.; Muryanto; Y.A.; Priyandoko, D.; Sari, A.A. Innovative chemically modified biosorbent for removal of procion red. *Int. J. Technol.* **2019**, *10*, 776-786, <https://doi.org/10.14716/ijtech.v10i4.2398>.
40. Belalia, M.; Bendjelloul, M.; Aziz, A.; Elandalousi, E.H. Surface modification of olive stone waste for enhanced sorption properties of cadmium and lead ions. *Acta chemica IASI* **2018**, *26*, 281-306, <https://doi.org/10.2478/achi-2018-0018>.
41. Li, X.; Li, Y. Preparation and modification of biomass carbon and research of the adsorption of copper. *IOP Conf. Series: Earth and Environmental Science* **2019**, *300*, 1-6, <https://doi.org/10.1088/1755-1315/300/5/052034>.
42. Muin, N.A.A.; Maarof, H.I.; Bashah, N.A.A.; Zubir, N.A.; Alrozi, R.; Nasuha, N. Electrochemical Removal of Copper Ions Using Coconut Shell Activated Carbon. *Indones. J. Chem.* **2020**, *20*, 530–535, <https://doi.org/10.22146/ijc.43077>.
43. Bhatnagar, A.; Sillanpää, M.; Witek-Krowrak, A. Agricultural waste peels as versatile biomass for water purification: A review. *Chem. Eng. J.* **2015**, *207*, 244–271, <https://doi.org/10.1016/j.cej.2015.01.135>.
44. Nuraqeelah, M.S.; Wee, B.S.; Chin, S.F.; Kok, K.Y. Synthesis and characterization of zinc oxide nanoparticles with small particle size distribution. *Acta Chimica Slovenica* **2018**, *65*, 578–585, <https://doi.org/10.17344/acsi.2018.4213>.
45. Zhou, M.; Wei, Z.; Qiao, H.; Zhu, L.; Yang, H.; Xia, T. Particle size and pore structure characterization of silver nanoparticles prepared by confined arc plasma. *J. Nanomater.* **2009**, *2009*, 1-5. <https://doi.org/10.1155/2009/968058>.
46. Droepenu, E.K.; Asare, E.A. Morphology of green synthesized ZnO nanoparticles using low temperature hydrothermal technique from aqueous *Carica papaya* extract. *Nanoscience and Nanotechnology* **2019**, *9*, 29-36.
47. Droepenu, E.K.; Boon, S.W.; Chin, S.F.; Kuan, Y.K.; Zaini, B.A.; Asare, E.A. Comparative evaluation of antibacterial efficacy of biological synthesis of ZnO nanoparticles using fresh leaf extract and fresh stem bark of *Carica papaya*. *Nano Biomed. Eng.* **2019**, *11*, 264-271, <https://doi.org/10.5101/nbe.v11i3.p264-271>.
48. Bai, X.; Li, L.; Liu, H.; Tan, L.; Liu, T.; Meng, X. Solvothermal synthesis of ZnO nanoparticles and anti-infection application in vivo. *ACS Applied Materials & Interface* **2015**, *7*, 1308–1317, <https://doi.org/10.1021/am507532p>.
49. Wang, Y.X.; Sun, J.; Yu, X.A. CTAB hydrothermal and solvothermal synthesis of ZnO nanopowders. *Ceramics International* **2011**, *37*, 3431–3436, <https://doi.org/10.1016/j.ceramint.2011.04.134>.
50. Cullity, B.D. *Elements of X-ray Diffractions*. Addison Wesley Publishing **1957**.
51. Sangkhaprom, N.; Supaphol, P.; Pavarajarn, V. Fibrous zinc oxide prepared by combined electrospinning and solvothermal techniques. *Ceramics International* **2010**, *36*, 357–360, <https://doi.org/10.1016/j.ceramint.2009.09.014>.
52. Wojnarowicz, J.; Opalinska, A.; Chudoba, T.; Gierlotka, S.; Mukhovskiy, R.; Pietrzykowska, E.; Sobczak, K.; Lojowski, W. Effect of Water Content in Ethylene Glycol Solvent on the Size of ZnO Nanoparticles Prepared Using Microwave Solvothermal Synthesis. *Journal of Nanomaterials* **2016**, *2016*, 1-15, <https://doi.org/10.1155/2016/2789871>.
53. Al Othman, Z.A.; Hashem, A.; Habila, M.A. Kinetic, Equilibrium and Thermodynamic Studies of Cadmium (II) Adsorption by Modified Agricultural Wastes. *Molecules* **2011**, *16*, 10443-10456; <https://doi.org/10.3390/molecules161210443>.

54. Borhan, A.; Abdullah, N.A.; Rashidi, N.A.; Taha, M.F. Removal of Cu²⁺ and Zn²⁺ from single metal aqueous solution using rubber-seed shell based activated carbon. *Proced. Eng.* **2016**, *148*, 694–701, <https://doi.org/10.1016/j.proeng.2016.06.571>.
55. Sun, K.; Jiang, J.C. Preparation and characterization of activated carbon from rubber-seed shell by physical activation with steam. *Biomass. Bioenerg.* **2010**, *34*, 539–544, <https://doi.org/10.1016/j.biombioe.2009.12.020>.
56. Khoshhesab, Z.M.; Sarfaraz, M.; Asadabad, M.A. Preparation of ZnO Nanostructures by Chemical Precipitation Method. *Synthesis and Reactivity in Inorganic, Metal-Organic, and Nano-Metal Chemistry* **2011**, *41*, 814–819, <https://doi.org/10.1080/15533174.2011.591308>.
57. Peres, M.L.; Delucis, R.A.; Amico, S.C.; Gatto, D.A. Zinc oxide nanoparticles from microwave-assisted solvothermal process: Photocatalytic performance and use for wood protection against xylophagous fungus. *Nanomaterials and Nanotechnology* **2019**, *9*, 1–8, <https://doi.org/10.1177/1847980419876201>.
58. Joshi, S.; Pokharel, B.P. Preparation and characterization of activated carbon from Lapsi (Choerospondias axillaris) seed stone by chemical activation with potassium hydroxide. *J. Inst. Eng.* **2013**, *9*, 79–88, <https://doi.org/10.3126/jie.v9i1.10673>.
59. Pathania, D.; Sharma, S.; Singh, P. Removal of MB by adsorption onto activated carbon developed from Ficus carica bast. *Arab. J. Chem.* **2017**, *10*, 1445–1451, <https://doi.org/10.1016/j.arabjc.2013.04.021>.
60. Moniruzzaman, M.; Rahman, M.A.; Aktar, S.; Khan, M. Equilibrium and Kinetic Parameters Determination of Cr(VI) Adsorption by Hogla Leaves (Typha elephantina Roxb). *Int. J. Waste. Resour.* **2017**, *7*, 1–7, <https://doi.org/10.4172/2252-5211.1000301>.
61. Singha, B.; Das, S.K. Bisorption of Cr (VI) ions from aqueous solution: kinetics, equilibrium and thermodynamics and desorption studies. *Colloids and Surfaces B: Biointerface* **2011**, *84*, 221–232, <https://doi.org/10.1016/j.colsurfb.2011.01.004>.
62. Tan, C.H.C.; Sabar, S.; Hussin, M.H. Development of immobilized microcrystalline cellulose as an effective adsorbent for methylene blue dye removal. *S. Afr. J. Chem. Eng.* **2018**, *26*, 11–24, <https://doi.org/10.1016/j.sajce.2018.08.001>.
63. Aydin, H.; Bulut, Y.; Yerlikaya, C. Removal of copper (II) from aqueous solution by adsorption onto low-cost adsorbents. *J. Environmental Management* **2008**, *87*, 37–45, <https://doi.org/10.1016/j.jenvman.2007.01.005>.
64. Akar, S.T.; Ozcan, A.S.; Akar, T.; Ozcan, A.; Kaynak, Z. Biosorption of a reactive textile dye from aqueous solutions utilizing an agrowaste. *Desalination* **2009**, *249*, 757–761, <https://doi.org/10.1016/j.desal.2008.09.012>.
65. Bhatti, H.N.; Mumtaz, B.; Muhammad, A.H.; Nadeem, R. Removal of Zn (II) ions from aqueous solution using Moringa oleifera Lam (Horseradish Tree) biomass. *Process Biochemistry* **2007**, *42*, 547–553, <https://doi.org/10.1016/j.procbio.2006.10.009>.
66. Putra, W.P.; Kamari, A.; Yusoff, S.N.M.; Ishak, C.F.; Mohamed, A.; Hashim, N.; Isa, I.Md. Biosorption of Cu(II), Pb(II) and Zn(II) ions from aqueous solutions using selected waste materials: Adsorption and characterisation studies. *J. Encapsul. Adsorp. Sci.* **2014**, *4*, 25–35. <https://doi.org/10.4236/jeas.2014.41004>.
67. Reddy, D.; Seshaiiah, K.; Reddy, A.V.R.; Lee, S.M. Optimization of Cd(II), Cu(II) and Ni(II) biosorption by chemically modified Moringa oleifera leaves powder. *Carbohydr. Polym* **2010**, *88*, 1077–1086, <https://doi.org/10.1016/j.carbpol.2012.01.073>.
68. Parvin, S.; Biswas, B.K.; Rahman, M.A.; Rahman, M.H.; Anik, M.S.; Uddin, M.R. Study on adsorption of Congo red onto chemically modified egg shell membrane. *Chemosphere* **2019**, *236*, <https://doi.org/10.1016/j.chemosphere.2019.07.057>.
69. Lakherwal, D.; Rattan, V.K.; Singh, H.P. Studies on adsorption of nickel by activated carbon in a liquid fluidised bed reactor. *Canadian. Chem. Trans.* **2016**, *4*, 121–132, <https://doi.org/10.13179/canchemtrans.2016.04.01.0264>.
70. Agbozu, I.E.; Emoruwa, F.O. Batch adsorption of heavy metals (Cu, Pb, Fe, Cr and Cd) from aqueous solutions using coconut husk. *African Journal of Environmental Science and Technology* **2014**, *8*, 239–246, <https://doi.org/10.5897/AJEST2013.1577>.
71. Roulia, M.; Vassiliadis, A.A. Sorption characterization of a cationic dye retained by clays and perlite. *Microporous Mesoporous Materials* **2008**, *116*, <https://doi.org/10.1016/j.micromeso.2008.03.017>.
72. Desta, M.B. Batch adsorption experiments: Langmuir and Freundlich isotherm studies for the adsorption of textile metal ions onto Teff straw (Eragrostis tef) agricultural waste. *J. Thermodyn.* **2013**, *2013*, 1–6, <https://doi.org/10.1155/2013/375830>.
73. Gao, Y.; Li, Y.; Zhang, L.; Huang, H.; Hu, J.; Shah, S.M.; Su, X. Adsorption and removal of tetracycline antibiotics from aqueous solution by graphene oxide. *J. Colloid Interface Sci.* **2012**, *368*, 540–546, <https://doi.org/10.1016/j.jcis.2011.11.015>.
74. Lafi, R.; Hafiane, A. Removal of methyl orange (MO) from aqueous solution using cationic surfactants modified coffee waste (MCWs). *J. Taiwan Inst. Chem. Eng.* **2016**, *58*, 424–433, <https://doi.org/10.1016/j.jtice.2015.06.035>.

75. Vijayakumar, G.; Tamilarasan, R.; Dharmendirakumar, M. Adsorption, Kinetic, Equilibrium and Thermodynamic studies on the removal of basic dye Rhodamine-B from aqueous solution by the use of natural adsorbent perlite. *J. Mater. Environ. Sci.* **2012**, *3*, 157-170.